

Supplemental Material: Modeling, Detecting, and Tracking Freezing of Gait in Parkinson Disease using Inertial Sensors

G.V. Prateek, Isaac Skog, Marie E. McNeely, Ryan P. Duncan, Gammon M. Earhart, and Arye Nehorai

APPENDIX A DERIVATION: DETECTOR-I

Let \mathbf{y}^a , \mathbf{u}^a , \mathbf{v}^a , and $\boldsymbol{\alpha}^a$ denote the concatenation of the observed accelerometer signal vector, direction of the accelerometer vector without the gravity vector, direction of the gravity vector, and magnitude of the accelerometer vector, respectively. Then,

$$\begin{aligned}\mathbf{y}^a &= [(\mathbf{y}_k^a)^T, \dots, (\mathbf{y}_{k+N-1}^a)^T]^T \in \mathbb{R}^{3N \times 1}, \\ \mathbf{u}^a &= [(\mathbf{u}_k^a)^T, \dots, (\mathbf{u}_{k+N-1}^a)^T]^T \in \mathbb{R}^{3N \times 1}, \\ \mathbf{v}^a &= [(\mathbf{v}_k^a)^T, \dots, (\mathbf{v}_{k+N-1}^a)^T]^T \in \mathbb{R}^{3N \times 1}, \\ \boldsymbol{\alpha}^a &= [\alpha_k^a, \dots, \alpha_{k+N-1}^a]^T \in \mathbb{R}^{N \times 1}.\end{aligned}$$

Under \mathcal{H}_0 , the conditional probability density function of \mathbf{y}^a , denoted as $f_0(\mathbf{y}^a | \boldsymbol{\alpha}^a, \mathbf{u}^a, \mathbf{v}^a)$ factors as

$$f_0(\mathbf{y}^a | \boldsymbol{\alpha}^a, \mathbf{u}^a, \mathbf{v}^a) = \prod_{k \in \Omega_N} \mathcal{N}(\alpha_k^a \mathbf{u}_k^a + g \mathbf{v}_k^a, \sigma_a^2 \mathbf{I}_3)$$

Under $\mathcal{H}_{1,2}$, the conditional probability density function of \mathbf{y} , denoted as $f_{1,2}(\mathbf{y} | \boldsymbol{\alpha}^a, \mathbf{u}^a, \mathbf{v}^a)$ factors as

$$f_{1,2}(\mathbf{y} | \boldsymbol{\alpha}^a, \mathbf{u}^a, \mathbf{v}^a) = \prod_{k \in \Omega_N} \mathcal{N}(\alpha_k^a \mathbf{u}^a + g \mathbf{v}^a, \sigma_a^2 \mathbf{I}_3)$$

The GLRT based detector replaces the unknown parameters with their maximum likelihood estimates (MLEs). Let $L_0(\boldsymbol{\alpha}^a, \mathbf{u}^a, \mathbf{v}^a | \mathbf{y}^a)$ and $L_{1,2}(\boldsymbol{\alpha}^a, \mathbf{u}^a, \mathbf{v}^a | \mathbf{y}^a)$ denote the log-likelihood of the probability distribution functions under \mathcal{H}_0 and $\mathcal{H}_{1,2}$, respectively. If $L_{D_1}(\mathbf{y}^a)$ is the likelihood ratio, and $\hat{\boldsymbol{\alpha}}^a$, $\hat{\mathbf{u}}^a$, and $\hat{\mathbf{v}}^a$, are the maximum likelihood estimates of the unknown parameters, then the GLRT based detector can be written as

$$\begin{aligned}\ln L_{D_1}(\mathbf{y}^a) &= \max_{\boldsymbol{\alpha}^a, \mathbf{u}^a, \mathbf{v}^a} L_0(\boldsymbol{\alpha}^a, \mathbf{u}^a, \mathbf{v}^a | \mathbf{y}^a) \\ &\quad - \max_{\boldsymbol{\alpha}^a, \mathbf{u}^a, \mathbf{v}^a} L_{1,2}(\boldsymbol{\alpha}^a, \mathbf{u}^a, \mathbf{v}^a | \mathbf{y}^a) \stackrel{\mathcal{H}_0}{\geq} \ln \gamma_{D_1}.\end{aligned}\quad (\text{A.1})$$

The loglikelihood function, $L_0(\boldsymbol{\alpha}^a, \mathbf{u}^a, \mathbf{v}^a | \mathbf{y}^a)$, under the hypothesis \mathcal{H}_0 , is

$$L_0(\boldsymbol{\alpha}^a, \mathbf{u}^a, \mathbf{v}^a | \mathbf{y}^a) = c - \sum_{k \in \Omega_N} \left[\frac{1}{2\sigma_a^2} \|\mathbf{y}_k^a - \alpha_k^a \mathbf{u}_k^a - g \mathbf{v}_k^a\|^2 \right],$$

where c is the normalizing constant. However, the parameters α_k^a , \mathbf{u}_k^a , and \mathbf{v}_k^a that define the accelerometer signal are unknown. Hence, the maximum of the $L_0(\boldsymbol{\alpha}^a, \mathbf{u}^a, \mathbf{v}^a | \mathbf{y}^a)$ is,

$$\max_{\boldsymbol{\alpha}^a, \mathbf{u}^a, \mathbf{v}^a} L_0(\boldsymbol{\alpha}^a, \mathbf{u}^a, \mathbf{v}^a | \mathbf{y}^a) = c. \quad (\text{A.2})$$

The loglikelihood function, $L_{1,2}(\boldsymbol{\alpha}^a, \mathbf{u}^a, \mathbf{v}^a | \mathbf{y}^a)$, under the hypothesis $\mathcal{H}_{1,2}$ is given as:

$$L_{1,2}(\boldsymbol{\alpha}^a, \mathbf{u}^a, \mathbf{v}^a | \mathbf{y}^a) = c - \sum_{k \in \Omega_N} \left[\frac{1}{2\sigma_a^2} \|\mathbf{y}_k^a - \alpha_k^a \mathbf{u}^a - g \mathbf{v}^a\|^2 \right]. \quad (\text{A.3})$$

Let $\hat{\alpha}_k^a$ be the MLE of α_k^a that minimizes (A.3). Taking the partial derivative with respect to α_k^a and equating it to zero, we get

$$\hat{\alpha}_k^a = \frac{(\mathbf{u}^a)^T (\mathbf{y}_k^a - g \mathbf{v}^a)}{\|\mathbf{u}^a\|^2} = (\mathbf{u}^a)^T (\mathbf{y}_k^a - g \mathbf{v}^a). \quad (\text{A.4})$$

Substituting (A.4) in (A.3) gives

$$\begin{aligned}L_{1,2}(\hat{\boldsymbol{\alpha}}^a, \mathbf{u}^a, \mathbf{v}^a | \mathbf{y}^a) &= c - \\ &\quad \frac{1}{2\sigma_a^2} \sum_{k \in \Omega_N} \|\mathbf{y}_k^a - (\mathbf{u}^a)^T (\mathbf{y}_k^a - g \mathbf{v}^a) - g \mathbf{v}^a\|^2.\end{aligned}\quad (\text{A.5})$$

Maximizing (A.5) is equivalent solving the following minimization problem:

$$\min_{\mathbf{u}^a, \mathbf{v}^a} \sum_{k \in \Omega_N} \|\mathbf{y}_k^a - g \mathbf{v}^a\|_{\mathbf{P}_{\mathbf{u}^a}^\perp}^2, \quad (\text{A.6})$$

where $\mathbf{P}_{\mathbf{u}^a}^\perp = \mathbf{I} - \mathbf{u}^a (\mathbf{u}^a)^T$. Note that $\mathbf{P}_{\mathbf{u}^a}^\perp$ is idempotent and symmetric, which makes it an orthogonal projection matrix. The weighted optimization problem in (A.6) is bi-quadratic, i.e., it is quadratic with respect to both \mathbf{u}^a and \mathbf{v}^a . Further, the optimization problem in (A.6) does not have a closed form expression. Here, we use alternative minimization technique to solve (A.6). In alternative minimization, one of the two variables \mathbf{u}^a and \mathbf{v}^a is fixed, and minimizing the function with respect to the other variable is of low-complexity and high stability. We begin solving the optimization problem by first fixing \mathbf{v}^a in (A.6). The minimization problem is formulated as

$$\begin{aligned}\min_{\mathbf{u}^a} \sum_{k \in \Omega_N} \left\{ \|\mathbf{y}_k^a - g \mathbf{v}^a\|^2 - (\mathbf{y}_k^a - g \mathbf{v}^a)^T \mathbf{u}^a (\mathbf{u}^a)^T (\mathbf{y}_k^a - g \mathbf{v}^a) \right\} \\ = \max_{\mathbf{u}^a} \left\{ (\mathbf{u}^a)^T \sum_{k \in \Omega_N} [(\mathbf{y}_k^a - g \mathbf{v}^a)(\mathbf{y}_k^a - g \mathbf{v}^a)^T] \mathbf{u}^a \right\}.\end{aligned}\quad (\text{A.7})$$

Let $\mathbf{G}^a = \sum_{k \in \Omega_N} [(\mathbf{y}_k^a - g \mathbf{v}^a)(\mathbf{y}_k^a - g \mathbf{v}^a)^T]$. The matrix \mathbf{G}^a is positive definite and symmetric. Let $\hat{\mathbf{u}}^a$ denote the eigenvector corresponding to the maximum eigenvalue of \mathbf{G}^a . Equation (A.7) is maximized when \mathbf{u}^a is equal to the eigenvector corresponding to the maximum eigenvalue of \mathbf{G}^a . For any symmetric and positive semi-definite matrix, \mathbf{G}^a , the maximum eigenvector represents the direction of the semi-major axis, and its eigenvalue represents the length of the semi-major axis. Clearly, the eigenvector corresponding to the maximum eigenvalue of the outer product term in (A.7) captures the direction of the trembling because it subtracts the constant magnitude and direction representing the gravitational force from the accelerometer readings, and computes the outer product. If $\lambda_{\max}(\cdot)$ denotes the the maximum eigenvalue and $\tilde{\mathbf{u}}^a$ denotes the optimal value of \mathbf{u}^a , then

$$\tilde{\mathbf{u}}^a = \text{eigenvector corresponding to } \lambda_{\max}(\mathbf{G}^a). \quad (\text{A.8})$$

Next, we fix \mathbf{u}^a in (A.6) and minimize the objective function with respect to \mathbf{v}^a . The minimization problem is formulated as

$$\min_{\mathbf{v}^a} \sum_{k \in \Omega_N} \|\mathbf{y}_k^a - g\mathbf{v}^a\|_{\mathbf{P}_{\mathbf{u}^a}^\perp}^2. \quad (\text{A.9})$$

Taking the partial derivative of (A.9) with respect to \mathbf{v}^a and equating to zero we get

$$-2g \sum_{k \in \Omega_N} \mathbf{P}_{\mathbf{u}^a}^\perp (\mathbf{y}_k^a - g\mathbf{v}^a) = \mathbf{0}. \quad (\text{A.10})$$

If $\mathbf{P}_{\mathbf{u}^a}$ represents the projection matrix that is orthogonal to $\mathbf{P}_{\mathbf{u}^a}^\perp$, then based on the orthogonality of projection matrices, we get $\sum_{k \in \Omega_N} (\mathbf{y}_k^a - g\mathbf{v}^a) \in \mathbf{P}_{\mathbf{u}^a}$. This implies that $\sum_{k \in \Omega_N} (\mathbf{y}_k^a - g\mathbf{v}^a) = \eta \mathbf{u}^a$, where $\eta > 0$ is the magnitude of the unit vector in the direction of \mathbf{u}^a . The choice of $\eta > 0$ can be arbitrary since we are only concerned with the direction of the unit vector \mathbf{v}^a . Here, we choose $\eta = 1$. Therefore, we get

$$\sum_{k \in \Omega_N} (\mathbf{y}_k^a - g\mathbf{v}^a) = \mathbf{u}^a. \quad (\text{A.11})$$

Solving for \mathbf{v}^a and ignoring the scale parameter, we get

$$\mathbf{v}^a = \frac{1}{N} \sum_{k \in \Omega_N} (\mathbf{y}_k^a - \bar{\mathbf{u}}^a) = (\bar{\mathbf{y}}_k^a - \bar{\mathbf{u}}^a). \quad (\text{A.12})$$

In (A.12), the trembling axis is subtracted from every sample of the accelerometer to obtain the direction of the gravitational vector. Let $\tilde{\mathbf{v}}^a$ denote the unit norm vector in the direction of \mathbf{v}^a . In Algorithm 1, we summarize the steps of the alternating minimization approach to find the MLE of \mathbf{u}^a and \mathbf{v}^a . Substituting $\hat{\mathbf{u}}^a$ and $\hat{\mathbf{v}}^a$ in (A.5), we get

Algorithm 1 Alternating Minimization

Initialize: $i = 0$, $C_{(0)} = 0$, ϵ , and I

Initialize: $\mathbf{v}_{(0)}^a = \bar{\mathbf{y}}_k^a / \|\bar{\mathbf{y}}_k^a\|$, where $\bar{\mathbf{y}}_k^a = (1/N) \sum_{k \in \Omega_N} \mathbf{y}_k^a$

- 1: **while** ($i \leq I$) and ($|C_{(i)} - C_{(i-1)}| < \epsilon$) **do**
 - 2: $\mathbf{G}_{(i)}^a \leftarrow \sum_{k \in \Omega_N} [(\mathbf{y}_k^a - g\mathbf{v}_{(i-1)}^a)(\mathbf{y}_k^a - g\mathbf{v}_{(i-1)}^a)^T]$
 - 3: $\tilde{\mathbf{u}}_{(i)}^a \leftarrow$ eigenvector corresponding to $\lambda_{\max}(\mathbf{G}_{(i)}^a)$
 - 4: $(\bar{\mathbf{y}}_k^a - \bar{\mathbf{u}}_{(i)}^a) \leftarrow \frac{1}{N} \sum_{k \in \Omega_N} (\mathbf{y}_k^a - \mathbf{u}_{(i)}^a)$
 - 5: $\tilde{\mathbf{v}}_{(i)}^a \leftarrow (\bar{\mathbf{y}}_k^a - \bar{\mathbf{u}}_{(i)}^a) / \|\bar{\mathbf{y}}_k^a - \bar{\mathbf{u}}_{(i)}^a\|$
 - 6: $C_{(i)} \leftarrow \sum_{k \in \Omega_N} (\mathbf{y}_k^a - g\tilde{\mathbf{v}}_{(i)}^a)^T \mathbf{P}_{\tilde{\mathbf{u}}_{(i)}^a}^\perp (\mathbf{y}_k^a - g\tilde{\mathbf{v}}_{(i)}^a)$
 - 7: $i \leftarrow i + 1$
 - 8: **end while**
 - 9: **return** $\hat{\mathbf{u}}^a = \tilde{\mathbf{u}}_{(i)}^a$ and $\hat{\mathbf{v}}^a = \tilde{\mathbf{v}}_{(i)}^a$
-

$$L_{1,2}(\hat{\alpha}^a, \hat{\mathbf{u}}^a, \hat{\mathbf{v}}^a | \mathbf{y}^a) = c - \frac{1}{2\sigma_a^2} \sum_{k \in \Omega_N} \|\mathbf{y}_k^a - g\hat{\mathbf{v}}^a\|_{\mathbf{P}_{\hat{\mathbf{u}}^a}^\perp}^2. \quad (\text{A.13})$$

Substituting (A.2) and (A.13) in (A.1), we get

$$\ln L_{D_1}(\mathbf{y}^a) = \frac{1}{2\sigma_a^2} \sum_{k \in \Omega_N} \|\mathbf{y}_k^a - g\hat{\mathbf{v}}^a\|_{\mathbf{P}_{\hat{\mathbf{u}}^a}^\perp}^2. \quad (\text{A.14})$$

The test statistic, $T_{D_1}(\mathbf{y}^a) = (2/N) \ln L_{D_1}(\mathbf{y}^a)$, is given as

$$T_{D_1}(\mathbf{y}^a) = \frac{1}{N} \sum_{k \in \Omega_N} \left\{ \frac{1}{\sigma_a^2} \|\mathbf{y}_k^a - g\hat{\mathbf{v}}^a\|_{\mathbf{P}_{\hat{\mathbf{u}}^a}^\perp}^2 \right\}^{\mathcal{H}_{1,2}} < \gamma'_{D_1}, \quad (\text{A.15})$$

where $\gamma'_{D_1} = (2/N) \ln \gamma_{D_1}$.

APPENDIX B DERIVATION: DETECTOR-II

Let \mathbf{y}^ω , \mathbf{u}^ω , and β^ω denote the concatenation of the observed gyroscope signal vector, direction of the gyroscope vector, and magnitude of the gyroscope vector, respectively. Then,

$$\begin{aligned} \mathbf{y}^\omega &= [(\mathbf{y}_k^\omega)^T, \dots, (\mathbf{y}_{k+N-1}^\omega)^T]^T \in \mathbb{R}^{3N \times 1}, \\ \mathbf{u}^\omega &= [(\mathbf{u}_k^\omega)^T, \dots, (\mathbf{u}_{k+N-1}^\omega)^T]^T \in \mathbb{R}^{3N \times 1}, \\ \beta^\omega &= [\beta_k^\omega, \dots, \beta_{k+N-1}^\omega]^T \in \mathbb{R}^{N \times 1}. \end{aligned}$$

where $s_k^\omega = \beta_k^\omega \mathbf{u}_k^\omega$, β_k^ω is the magnitude of the angular velocity vector, and \mathbf{u}_k^ω is a unit vector in the direction of the angular velocity vector. Let $\mathbf{y} = [(\mathbf{y}^a)^T, (\mathbf{y}^\omega)^T]^T$ denote the concatenation of the accelerometer and gyroscope signal. Under \mathcal{H}_1 , the conditional probability density function of \mathbf{y} , denoted as $f_1(\mathbf{y} | \mathbf{v}^a)$ factors as

$$f_1(\mathbf{y} | \mathbf{v}^a) = \prod_{k \in \Omega_N} \mathcal{N}(g\mathbf{v}^a, \sigma_a^2 \mathbf{I}_3) \times \mathcal{N}(\mathbf{0}, \sigma_\omega^2 \mathbf{I}_3).$$

Under \mathcal{H}_2 , the conditional probability density function of \mathbf{y} , denoted as $f_2(\mathbf{y} | \alpha^a, \mathbf{u}^a, \mathbf{v}^a, \beta^\omega, \mathbf{u}^\omega)$ factors as

$$\begin{aligned} f_2(\mathbf{y} | \alpha^a, \mathbf{u}^a, \mathbf{v}^a, \beta^\omega, \mathbf{u}^\omega) &= \prod_{k \in \Omega_N} \mathcal{N}(\alpha_k^a \mathbf{u}^a + g\mathbf{v}^a, \sigma_a^2 \mathbf{I}_3) \\ &\quad \times \mathcal{N}(\beta_k^\omega \mathbf{u}_k^\omega, \sigma_\omega^2 \mathbf{I}_3). \end{aligned}$$

Let $L_2(\alpha^a, \mathbf{u}^a, \mathbf{v}^a, \beta^\omega, \mathbf{u}^\omega | \mathbf{y})$ and $L_1(\mathbf{v}^a | \mathbf{y})$ denote the log-likelihood of the probability distribution functions under \mathcal{H}_2 and \mathcal{H}_1 , respectively. Let $L_{D_2}(\mathbf{y})$ denote the likelihood ratio, and $\hat{\alpha}^a$, $\hat{\mathbf{u}}^a$, $\hat{\mathbf{v}}^a$, $\hat{\beta}^a$, and $\hat{\mathbf{u}}^\omega$ are the maximum likelihood estimates of the unknown parameters, then the GLRT based detector can be written as

$$\begin{aligned} \ln L_{D_2}(\mathbf{y}) &= \max_{\alpha^a, \mathbf{u}^a, \mathbf{v}^a, \beta^\omega, \mathbf{u}^\omega} L_2(\alpha^a, \mathbf{u}^a, \mathbf{v}^a, \beta^\omega, \mathbf{u}^\omega | \mathbf{y}) \\ &\quad - \max_{\mathbf{v}^a} L_1(\mathbf{v}^a | \mathbf{y}) \stackrel{\mathcal{H}_2}{\underset{\mathcal{H}_1}{\geq}} \ln \gamma_{D_2}. \end{aligned} \quad (\text{B.1})$$

The loglikelihood function, $L_2(\alpha^a, \mathbf{u}^a, \mathbf{v}^a, \beta^\omega, \mathbf{u}^\omega | \mathbf{y})$, under the hypothesis \mathcal{H}_2 , is

$$\begin{aligned} L_2(\alpha^a, \mathbf{u}^a, \mathbf{v}^a, \beta^\omega, \mathbf{u}^\omega | \mathbf{y}) &= c' - \\ &\quad \sum_{k \in \Omega_N} \left[\frac{1}{2\sigma_a^2} \|\mathbf{y}_k^a - \alpha_k^a \mathbf{u}^a - g\mathbf{v}^a\|^2 + \frac{1}{2\sigma_\omega^2} \|\mathbf{y}_k^\omega - \beta_k^\omega \mathbf{u}_k^\omega\|^2 \right]. \end{aligned}$$

where c' is a normalizing constant. The minimization of the third term with respect to α_k^a , \mathbf{u}^a , and \mathbf{v}^a follows the same steps as in Appendix A. In the fourth term, the parameters, β_k^ω and \mathbf{u}_k^ω , that describe the gyroscope vector are unknown and goes to the minimum value when the norm in the fourth term of (B.1) goes to zero. Hence, the maximum of the $L_2(\alpha^a, \mathbf{u}^a, \mathbf{v}^a, \beta^\omega, \mathbf{u}^\omega | \mathbf{y})$ is,

$$\begin{aligned} \max_{\alpha^a, \mathbf{u}^a, \mathbf{v}^a, \beta^\omega, \mathbf{u}^\omega} L_2(\alpha^a, \mathbf{u}^a, \mathbf{v}^a, \beta^\omega, \mathbf{u}^\omega | \mathbf{y}) \\ = c' - \frac{1}{2\sigma_a^2} \sum_{k \in \Omega_N} \|\mathbf{y}_k^a - g\hat{\mathbf{v}}^a\|_{\mathbf{P}_{\hat{\mathbf{u}}^a}^\perp}^2. \end{aligned} \quad (\text{B.2})$$

The loglikelihood function, $L_1(\mathbf{v}^a|\mathbf{y})$, under the hypothesis \mathcal{H}_1 , is

$$L_1(\mathbf{v}^a|\mathbf{y}) = c' - \sum_{k \in \Omega_N} \left[\frac{1}{2\sigma_a^2} \|\mathbf{y}_k^a - g\mathbf{v}^a\|^2 + \frac{1}{2\sigma_\omega^2} \|\mathbf{y}_k^\omega\|^2 \right].$$

If $\hat{\mathbf{v}}^a$ represents the maximum likelihood estimate of \mathbf{v}^a , then,

$$\hat{\mathbf{v}}^a = \frac{\bar{\mathbf{y}}^a}{\|\bar{\mathbf{y}}^a\|}, \quad \text{where } \bar{\mathbf{y}}^a = \frac{1}{N} \sum_{k \in \Omega_N} \mathbf{y}_k^a. \quad (\text{B.3})$$

Hence, the maximum of $L_1(\mathbf{v}^a|\mathbf{y})$ is given as

$$\begin{aligned} \max_{\mathbf{v}^a} L_1(\mathbf{v}^a|\mathbf{y}) &= c' \\ &- \sum_{k \in \Omega_N} \left[\frac{1}{2\sigma_a^2} \left\| \mathbf{y}_k^a - g \frac{\bar{\mathbf{y}}^a}{\|\bar{\mathbf{y}}^a\|} \right\|^2 + \frac{1}{2\sigma_\omega^2} \|\mathbf{y}_k^\omega\|^2 \right]. \end{aligned} \quad (\text{B.4})$$

Substituting (B.2) and (B.4) into (B.1), we get

$$\begin{aligned} \ln L_{D_2}(\mathbf{y}) &= \sum_{k \in \Omega_N} \left[\frac{1}{2\sigma_a^2} \left\| \mathbf{y}_k^a - g \frac{\bar{\mathbf{y}}^a}{\|\bar{\mathbf{y}}^a\|} \right\|^2 \right. \\ &\quad \left. - \frac{1}{2\sigma_a^2} \|\mathbf{y}_k^a - g\hat{\mathbf{v}}^a\|_{\mathbf{P}_{\hat{\mathbf{v}}^a}^\perp}^2 + \frac{1}{2\sigma_\omega^2} \|\mathbf{y}_k^\omega\|^2 \right]. \end{aligned} \quad (\text{B.5})$$

If loglikelihood ratio is denoted as $L_{D_2}(\mathbf{y})$, then the test statistic, $T_{D_2}(\mathbf{y}) = (2/N) \ln L_{D_2}(\mathbf{y})$, is given as

$$\begin{aligned} T_{D_2}(\mathbf{y}) &= \frac{1}{N} \sum_{k \in \Omega_N} \left\{ \frac{1}{\sigma_\omega^2} \|\mathbf{y}_k^\omega\|^2 \right. \\ &\quad \left. + \frac{1}{\sigma_a^2} \left[\left\| \mathbf{y}_k^a - g \frac{\bar{\mathbf{y}}^a}{\|\bar{\mathbf{y}}^a\|} \right\|^2 - \|\mathbf{y}_k^a - g\hat{\mathbf{v}}^a\|_{\mathbf{P}_{\hat{\mathbf{v}}^a}^\perp}^2 \right] \right\} \stackrel{\mathcal{H}_1}{<} \gamma'_{D_2}, \end{aligned} \quad (\text{B.6})$$

where $\gamma'_{D_2} = (2/N) \ln \gamma_{D_2}$.

APPENDIX C DERIVATION: POINT-PROCESS FILTER

In this section, we derive the stochastic state point process filter when the observation model follows a binomial distribution. The derivation follows similar steps to those stated in [52]. We approximate the posterior distribution in (12) to a Gaussian distribution. Under this approximation, the mean and variance of the one-step predication density in (13) are computed from the posterior density in the previous time interval as

$$\begin{aligned} \boldsymbol{\theta}_{k|k-1} &= \mathbf{F}_k \boldsymbol{\theta}_{k-1|k-1}, \\ \mathbf{P}_{k|k-1} &= \mathbf{F}_k \mathbf{P}_{k-1|k-1} \mathbf{F}_k^T + \mathbf{Q}_k. \end{aligned}$$

The posterior distribution in the time interval $((k-1)\Delta, k\Delta]$ is approximated as a Gaussian distribution with parameters $\boldsymbol{\theta}_{k|k}$ and $\mathbf{P}_{k|k}$ as the mean and variance, respectively. Let $L(\boldsymbol{\theta}_k)$ denote the loglikelihood of the posterior distribution without the normalizing constant, i.e., $L(\boldsymbol{\theta}_k) =$

$\ln(P(b_k|\boldsymbol{\theta}_k, \mathbf{H}_k)P(\boldsymbol{\theta}_k|\mathbf{H}_k))$. The second order expansion of the logarithm about a point $\hat{\boldsymbol{\theta}}_k$ gives

$$\begin{aligned} L(\boldsymbol{\theta}_k) &\approx L(\hat{\boldsymbol{\theta}}_k) + L'(\hat{\boldsymbol{\theta}}_k)(\boldsymbol{\theta}_k - \hat{\boldsymbol{\theta}}_k) \\ &\quad + \frac{1}{2}(\boldsymbol{\theta}_k - \hat{\boldsymbol{\theta}}_k)^T L''(\hat{\boldsymbol{\theta}}_k)(\boldsymbol{\theta}_k - \hat{\boldsymbol{\theta}}_k) \end{aligned} \quad (\text{C.1})$$

$$\begin{aligned} &= c'' + \frac{1}{2} \left[\boldsymbol{\theta}_k - \left\{ \hat{\boldsymbol{\theta}}_k - [L''(\hat{\boldsymbol{\theta}}_k)]^{-1} L'(\hat{\boldsymbol{\theta}}_k) \right\} \right]^T \times \\ &\quad L''(\hat{\boldsymbol{\theta}}_k) \left[\boldsymbol{\theta}_k - \left\{ \hat{\boldsymbol{\theta}}_k - [L''(\hat{\boldsymbol{\theta}}_k)]^{-1} L'(\hat{\boldsymbol{\theta}}_k) \right\} \right]. \end{aligned} \quad (\text{C.2})$$

The posterior is approximated as a Gaussian, distributed with $\boldsymbol{\theta}_{k|k}$ and $\mathbf{P}_{k|k}$ as the mean and variance, respectively, and is given as

$$\begin{aligned} \boldsymbol{\theta}_{k|k} &= \hat{\boldsymbol{\theta}}_k - [L''(\hat{\boldsymbol{\theta}}_k)]^{-1} L'(\hat{\boldsymbol{\theta}}_k) \\ \mathbf{P}_{k|k} &= -[L''(\hat{\boldsymbol{\theta}}_k)]^{-1}. \end{aligned} \quad (\text{C.3})$$

By evaluating (C.3) at $\hat{\boldsymbol{\theta}}_k = \boldsymbol{\theta}_{k|k-1}$, we get the posterior state equations. The first partial derivative of the loglikelihood function of the posterior distribution is given as:

$$\begin{aligned} L'(\boldsymbol{\theta}_k) &= \frac{\partial}{\partial \boldsymbol{\theta}_k} \left[\ln \binom{B}{b_k} + b_k \ln p_k + (B - b_k) \ln(1 - p_k) \right. \\ &\quad \left. - \frac{1}{2}(\boldsymbol{\theta}_k - \boldsymbol{\theta}_{k|k-1})^T (\mathbf{P}_{k|k-1})^{-1} (\boldsymbol{\theta}_k - \boldsymbol{\theta}_{k|k-1}) \right] \\ &= \left[\frac{b_k}{p_k} \frac{\partial p_k}{\partial \boldsymbol{\theta}_k} + \frac{B - b_k}{1 - p_k} \frac{\partial(1 - p_k)}{\partial \boldsymbol{\theta}_k} \right] \\ &\quad - (\mathbf{P}_{k|k-1})^{-1} (\boldsymbol{\theta}_k - \boldsymbol{\theta}_{k|k-1}). \end{aligned} \quad (\text{C.4})$$

From the definition of the p_k , which represents a sigmoid function, we obtain the following identities:

$$\frac{1}{p_k} \frac{\partial p_k}{\partial \boldsymbol{\theta}_k} = (1 - p_k) \frac{\partial \lambda_k(\boldsymbol{\theta}_k)}{\partial \boldsymbol{\theta}_k} \quad (\text{C.5})$$

$$\frac{1}{1 - p_k} \frac{\partial(1 - p_k)}{\partial \boldsymbol{\theta}_k} = -p_k \frac{\partial \lambda_k(\boldsymbol{\theta}_k)}{\partial \boldsymbol{\theta}_k}. \quad (\text{C.6})$$

Substituting (C.5) and (C.6) into (C.4) we get

$$L'(\boldsymbol{\theta}_k) = (b_k - Bp_k) \frac{\partial \lambda_k(\boldsymbol{\theta}_k)}{\partial \boldsymbol{\theta}_k} - (\mathbf{P}_{k|k-1})^{-1} (\boldsymbol{\theta}_k - \boldsymbol{\theta}_{k|k-1}). \quad (\text{C.7})$$

Taking the second derivative of (C.7), we get

$$\begin{aligned} L''(\boldsymbol{\theta}_k) &= -(\mathbf{P}_{k|k-1})^{-1} + (b_k - Bp_k) \frac{\partial^2 \lambda_k(\boldsymbol{\theta}_k)}{\partial \boldsymbol{\theta}_k \partial \boldsymbol{\theta}_k^T} \\ &\quad - \frac{\partial \lambda_k(\boldsymbol{\theta}_k)}{\partial \boldsymbol{\theta}_k} Bp_k(1 - p_k) \frac{\partial \lambda_k(\boldsymbol{\theta}_k)}{\partial \boldsymbol{\theta}_k}^T \end{aligned} \quad (\text{C.8})$$

Therefore, substituting the expressions of the first and second partial derivatives of the loglikelihood function in (C.7) and (C.8) into (C.3), and evaluating at $\boldsymbol{\theta}_k = \boldsymbol{\theta}_{k|k-1}$, we get

$$\begin{aligned} \boldsymbol{\theta}_{k|k} &= \boldsymbol{\theta}_{k|k-1} + \mathbf{P}_{k|k} \left[(b_k - Bp_k) \frac{\partial \lambda_k(\boldsymbol{\theta}_k)}{\partial \boldsymbol{\theta}_k} \right]_{\boldsymbol{\theta}_{k|k-1}}, \\ (\mathbf{P}_{k|k})^{-1} &= (\mathbf{P}_{k|k-1})^{-1} + \left[(Bp_k - b_k) \frac{\partial^2 \lambda_k(\boldsymbol{\theta}_k)}{\partial \boldsymbol{\theta}_k \partial \boldsymbol{\theta}_k^T} \right. \\ &\quad \left. + Bp_k(1 - p_k) \frac{\partial \lambda_k(\boldsymbol{\theta}_k)}{\partial \boldsymbol{\theta}_k} \frac{\partial \lambda_k(\boldsymbol{\theta}_k)}{\partial \boldsymbol{\theta}_k}^T \right]_{\boldsymbol{\theta}_{k|k-1}}. \end{aligned}$$

The analysis of the convergence of the point-process filter is presented in [53].

APPENDIX D
SYSTEM PARAMETERS: DETECTOR-I

Under $\mathcal{H}_{1,2}$, the distribution of the test statistic in (4) follows a chi-square distribution when \hat{u}^a and \hat{v}^a are estimated accurately. Each term in (7) follows a χ_1^2 distribution because $\text{rank}(\mathbf{P}_{\hat{u}^a}^\perp) = 1$ and $\mathbf{P}_{\hat{u}^a}^\perp$ is an idempotent matrix. The test statistic in (7) represents the sum of independent chi-square distributions with $\nu = 1$ degrees of freedom. Hence, (7) follows χ_N^2 distribution. The exact detection performance is given by $P_{\text{FA}} = \mathcal{Q}_{\chi_N^2}(\gamma'_{D_1})$, where γ'_{D_1} is the detection threshold of Detector-I for a given probability of false alarm, and $\mathcal{Q}_{\chi_N^2}$ is the right-tail probability for a chi-squared distribution with N degrees of freedom.

To obtain the threshold γ'_{D_1} , we consider 5 second IMU data for six different PD participants (TT004–BLOCK, TT006–NARROW, TT013–NARROW, TT015–NARROW, TT021–BLOCK, and TT027–BLOCK). The IMU data consists of either a specific type of FOG pattern (turning freeze for TT004–BLOCK and TT013–NARROW, initiation freeze for TT021–BLOCK and TT027–BLOCK) or no specific FOG pattern. ZVEI, FOG intervals, and other gait patterns are identified in the video and marked as ZVEI (video), FOG (video), and MOVE (video) respectively. The synchronization between the video and IMU data was done manually. We use the definitions of TPR and FAR in (15) to evaluate the performance of the Detector-I across different values of threshold γ'_{D_1} , using the ZVEI (video) and FOG (video) region as the reference. In Fig. 1, we plot the average value of TPR and $1 - \text{FAR}$ obtained across the six datasets. We observe that, as the Detector-I threshold increases, the average value of TPR increases because Detector-I includes both TREI and ZVEI. However, the average value of $1 - \text{FAR}$ decreases with the increase in the threshold because gait patterns that are modeled as neither ZVEI nor TREI, but contain similar energy information are also identified. Further, in Fig. 1, we do not observe a significant improvement in the average value of TPR across different window lengths, and increasing the window length only leads to increase in the computational load on the microprocessor. Considering these factors, we choose $\gamma'_{D_1} = 34.39$ for $N = 100$ because the average value of TPR curve shows minor improvement in performance on increasing the threshold beyond 34.39.

We use the same illustrative example as in Section VII but with an overlay of the ZVEI, FOG interval, and other gait patterns observed in the video data. In Fig. 2, the gray background region indicates FOG (video), blue background region indicates ZVEI (video), and yellow background region indicates other gait patterns denoted as MOVE (video). We choose the standard deviation of accelerometer $\sigma_a = 1.0$. Note that the standard deviation of the accelerometer only scales the test statistic in (4), and can be set to any positive value. In Fig. 2c, we plot the output of the detector for the test statistic in (4). The IMU region detected by the Detector-I includes ZVEI (video) and significant region of the FOG (video) interval. However, it also includes some gait patterns that are not associated with FOG.

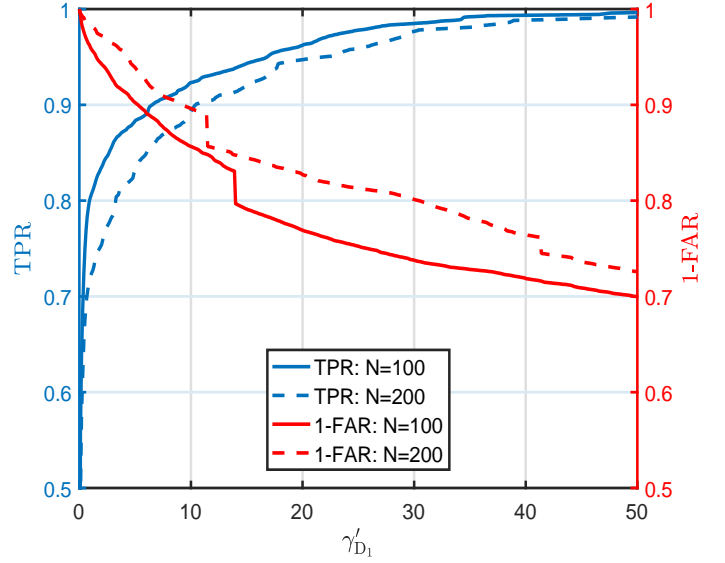


Fig. 1: Average value of TPR and $1 - \text{FAR}$ curves for different values of Detector-I threshold γ'_{D_1} .

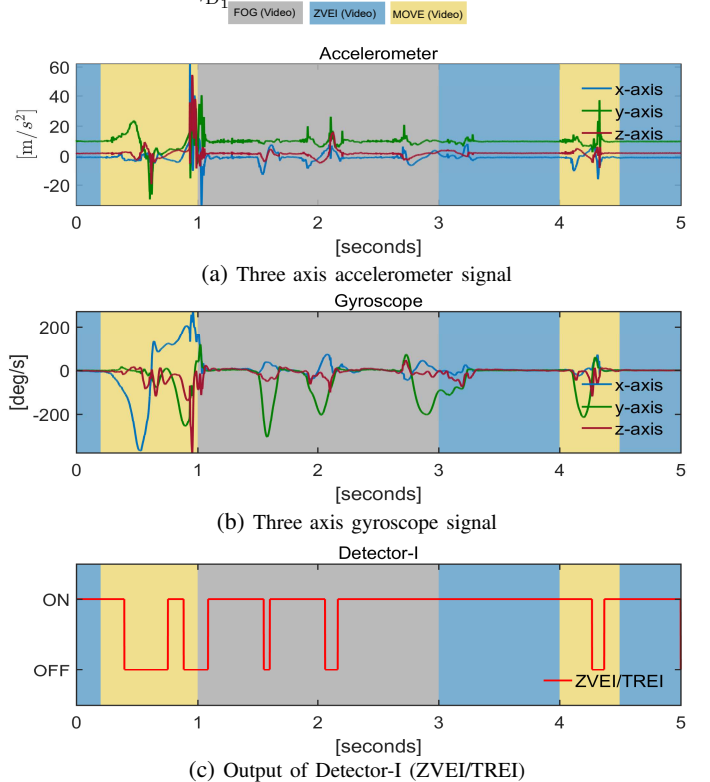


Fig. 2: Detector-I: Detected ZVEI or TREI with an overlay of the video data for TT004–BLOCK task.

APPENDIX E
SYSTEM PARAMETERS: DETECTOR-II

Under \mathcal{H}_1 , i.e., when the foot is stationary, the distribution of the test statistic in (7) again follows a chi-square distribution when \hat{u}^a and \hat{v}^a are estimated accurately. The difference between the second and third terms in (7) is approximately equal to zero, as each term indicates the energy due to the error measurements. As the test statistic in (7) is the sum of independent chi-squared distributions, each with $\nu = 1$,

the expression of the test statistic under \mathcal{H}_1 follows a χ_N^2 distribution. The exact detection performance is given by $P_{FA} = Q_{\chi_N^2}(\gamma'_{D_2})$, where γ'_{D_2} is the detection threshold of Detector-II for a given probability of false alarm.

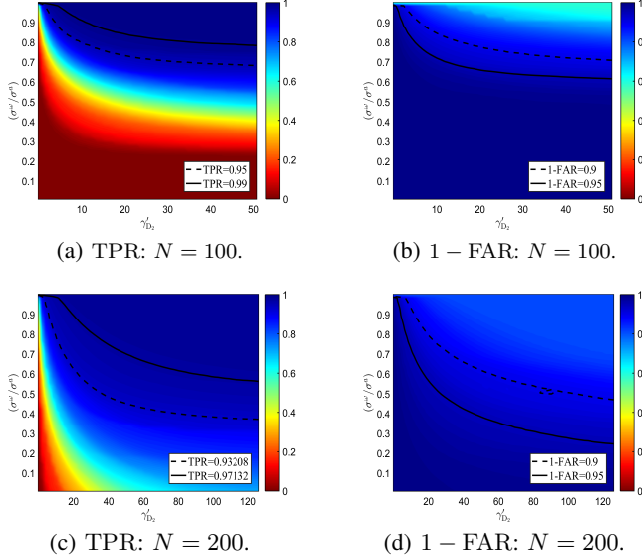


Fig. 3: Sensitivity of gyroscope: Image plots of average value of TPR and $1 - \text{FAR}$ for ZVEI across different values of Detector-II threshold and standard deviation of the gyroscope.

The sensitivity of the gyroscope is characterized σ_ω as it scales the test statistic in (7). To determine the sensitivity of the gyroscope signal, we plot the average values of TPR and $1 - \text{FAR}$ across different values of threshold γ'_{D_2} and σ_ω/σ_a with $\sigma_a = 1.0$. We use the same datasets as seen in the previous subsection. Since the goal of the Detector-II is to distinguish ZVEI from TREI, we compute the average values of TPR and $1 - \text{FAR}$ based on (15), with ZVEI (video) as the reference. We fix $N = 100$, $\sigma_a = 1.0$, and $\gamma'_{D_1} = 34.39$ for Detector-I, and observe the performance of the second detector. As the value of σ_ω goes to zero, the test statistic tends towards infinity and no ZVEI are detected for finite values of the Detector-II threshold. Therefore, for small values of σ_ω , the average value of TPR is close to zero, as observed in the lower half of Fig. 3a. Similarly, the lower half of Fig. 3b demonstrates no ZVEI for small values of σ_ω , or equivalently, $1 - \text{FAR}$ is one. As the sensitivity of the gyroscope and threshold γ'_{D_2} increase, the average value of TPR increases and $1 - \text{FAR}$ decreases. However, for a fixed large value of σ_ω/σ_a and beyond certain threshold (around $\gamma'_{D_2} = 10.0$ in Fig. 3a), the TPR curves begin to saturate. This saturation behavior is explained by the fact that the maximum region that the Detector-II can detect is bounded by the ZVEI/TREI detected by the Detector-I. We represent the regions with high average TPR (95 – 99%) and $1 - \text{FAR}$ (90 – 95%) values with solid-line and dashed-line plot, respectively. In particular, we set $\sigma_\omega/\sigma_a = 0.8$ for $N = 100$ which lies in 95 – 99% region of the average TPR plot and 90 – 95% region of the average $1 - \text{FAR}$ plot. However, due to the saturation behavior of the average value of TPR curve, the threshold γ'_{D_2} can take many finite values.

To determine the optimal threshold γ'_{D_2} , we compute the performance of the foot-mounted inertial navigation system

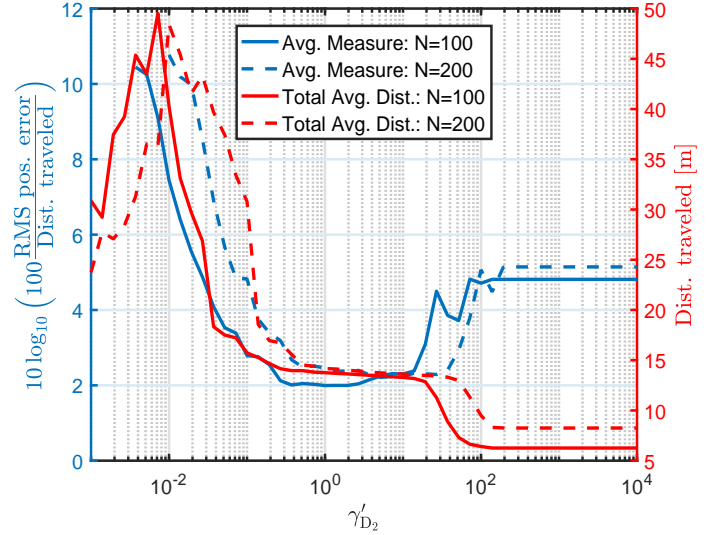


Fig. 4: Performance of the foot-mounted inertial navigation system plot across different value of the threshold.

for the calibration task. In the calibration task, the participant was asked to walk forward along a full 6 meter straight path. On reaching the end, the participant made a 180° turn and returned to the starting point. Each calibration task contains two datasets where the participant was asked to follow the same trajectory twice. The starting point and ending of the trajectory are the same and the total average distance traveled varied between 13.0-13.5 meters because the participants took an extra step or two beyond the physically marked end-point to complete the first turn. We compute the ratio of the root mean square (RMS) of the position error and distance traveled as follows [54]

$$10 \log_{10} \left(100 \frac{\text{RMS position error}}{\text{Distance traveled}} \right) \quad (\text{E.1})$$

where the root mean square of the position error is defined as the distance between the starting and ending point of the trajectory during the calibration task, and the distance traveled

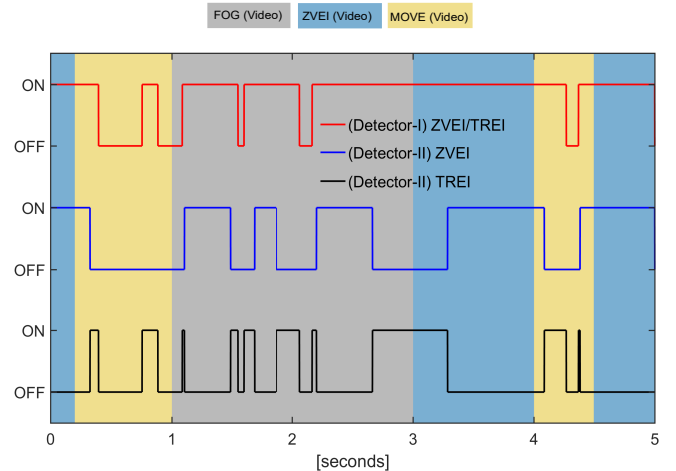


Fig. 5: State diagram of Detector-I and Detector-II for PID TT004-BLOCK task with an overlay of the video data.

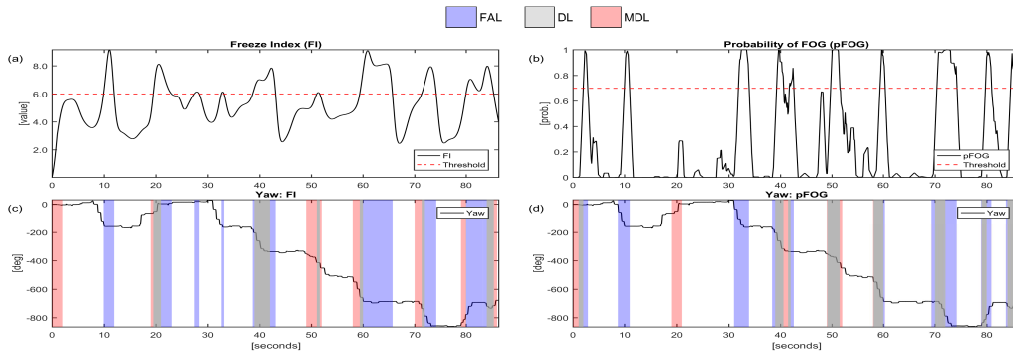


Fig. 6: PID TT027-BLOCK. (a) Freeze-Index plot with FI-threshold set to 6.0. (b) pFOG plot with $\sigma_s = 0.29$. (c) and (d) Yaw angle plot with an overlay of DL, MDL, and FAL. FOG region was marked using video data the following video commentary: Froze when stood up from chair to walk to block. Froze when turning to go back to cones after second trial. Froze during turn in the fourth, fifth, and sixth trials. Questionable left foot freeze in turn for seventh and eighth trials. Froze after trials over while walking away.

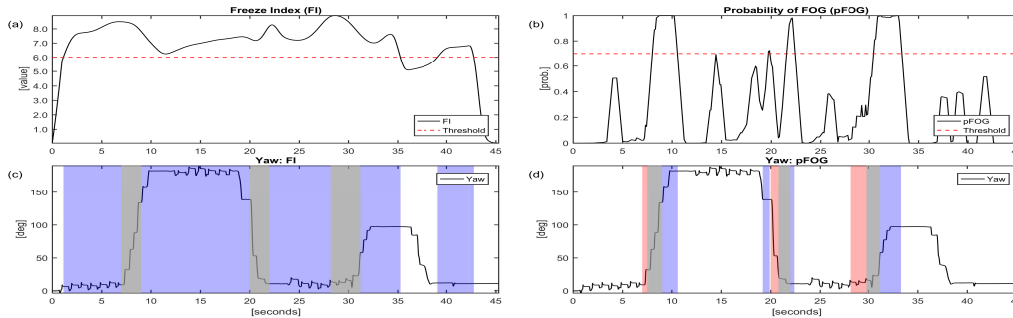


Fig. 7: PID TT027-BACK. (a) Freeze-Index plot with FI-threshold set to 6.0. (b) pFOG plot with $\sigma_s = 0.29$. (c) and (d) Yaw angle plot with an overlay of DL, MDL, and FAL. FOG region marked using the following video commentary: Froze turning after first backward trial. Froze turning after second backward trial. Froze at the end of third backward trial into a turn.

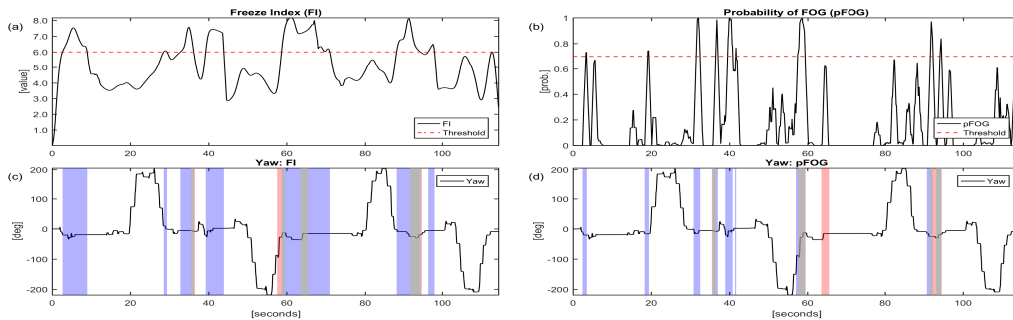


Fig. 8: PID TT027-EIGHT. (a) Freeze-Index plot with FI-threshold set to 6.0. (b) pFOG plot with $\sigma_s = 0.29$. (c) and (d) Yaw angle plot with an overlay of DL, MDL, and FAL. FOG region was marked using the following video commentary: Gait initiation freeze when standing up to start figure EIGHT trial, and first and second figure EIGHT trials. Froze during turn after second figure EIGHT trial. Froze when lining up for third and fourth figure EIGHT trials. The first two FOG events were not recorded in the IMU data.

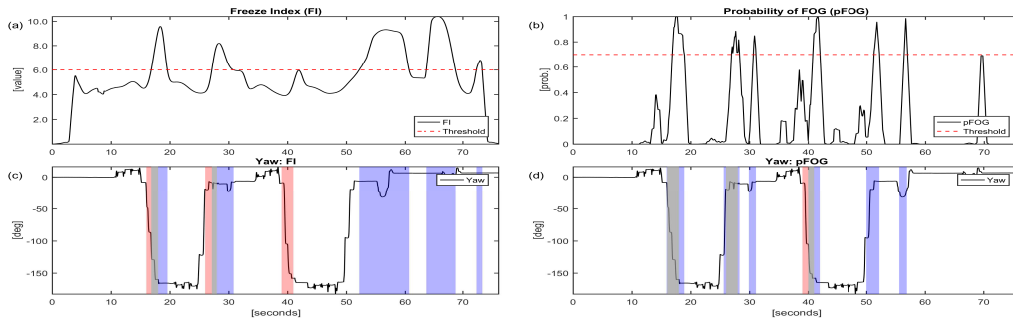


Fig. 9: PID TT027-NARROW. (a) Freeze-Index plot with FI-threshold set to 6.0. (b) pFOG plot with $\sigma_s = 0.29$. (c) and (d) Yaw angle plot with an overlay of DL, MDL, and FAL. FOG region was marked using the following video commentary: Froze when standing up and initiating gait to measure NARROW chair width. Froze during turn after first and third NARROW trials. Froze before side-step to line up for third NARROW trial. The first FOG event was not recorded in the IMU data.

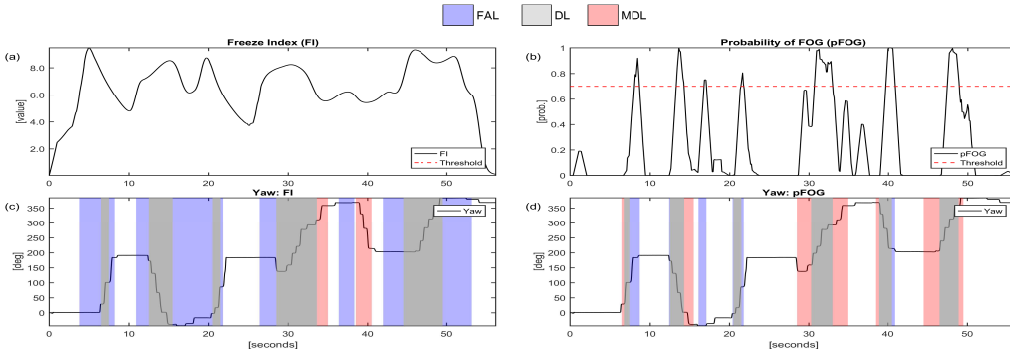


Fig. 10: PID TT027-TURN. (a) Freeze-Index plot with FI-threshold set to 6.0. (b) pFOG plot with $\sigma_s = 0.29$. (c) and (d) Yaw angle plot with an overlay of DL, MDL, and FAL. FOG region was marked using the following video commentary: Froze during first turn, twice during second turn, and third TURN trials. Froze turning wrong way in fourth TURN trial and then froze again turning correct way. Froze in the fifth and sixth TURN trials.

is defined as the sum of the distances between the position coordinates at the edges of the ZVEI during OFF state. When the threshold of Detector-II is set to a low value, no ZVEI are observed. In this case, the total distance measured by the system sums to zero, and the performance of the inertial navigation system in (E.1) is not defined, as shown in the left half of Fig. 4. When the threshold is set to a very high value, zero-velocity update is always ON and the ZVEI detected by Detector-II is equal to the ZVEI/TREI identified by the Detector-I. Due to this, the total distance is a non-zero value close to zero and the curve representing equation (E.1) saturates. The optimal performance of the inertial navigation system is obtained at the threshold when the curve in (E.1) attains the minimum value and the estimated total average distance is within an error-bound region of the true average distance. In Fig. 4, for $N = 100$, (E.1) attains a minimum at $\gamma'_{D_2} = 2.00$ and the average distance traveled is equal to 13.5 meters, which lies within the error-bound region.

In Fig. 5, we explain the behavior of the curves in Fig. 3 and Fig. 4 for the same illustrative example seen in Section VII. We set the system parameters $N = 100$, $\sigma_a = 1.00$, $\sigma_\omega = 0.8$, $\gamma'_{D_1} = 34.39$, and $\gamma'_{D_2} = 2.00$. The red curve indicates the output of Detector-I based on the test statistic in (4) and threshold γ'_{D_1} . The goal of Detector-II is to determine the ZVEI when Detector-I is ON. The blue curve represents the output of Detector-II for the test statistic in (7) and threshold γ'_{D_2} . In Fig. 5, we observe that there is a significant overlap between the ZVEI identified by the Detector-II and ZVEI (video) indicated with blue background. In addition, the FOG region detected in the video contains both ZVEI and TREI, because the turn freeze included both trembling and short stride lengths. However, Detector-II also identifies updates which contains similar energy information as TREI and are not associated with FOG.

APPENDIX F SUMMARY: PID TT027

In this section, we demonstrate the performance of the FI [19] and pFOG method for PID TT027, who demonstrated the greatest number of FOG events (24 in total). As the list of balance assessment tasks involved in place and sharp 180° turns, we overlay the DL, MDL, and FAL region detected on the yaw angle plot provided by the inertial navigation system.

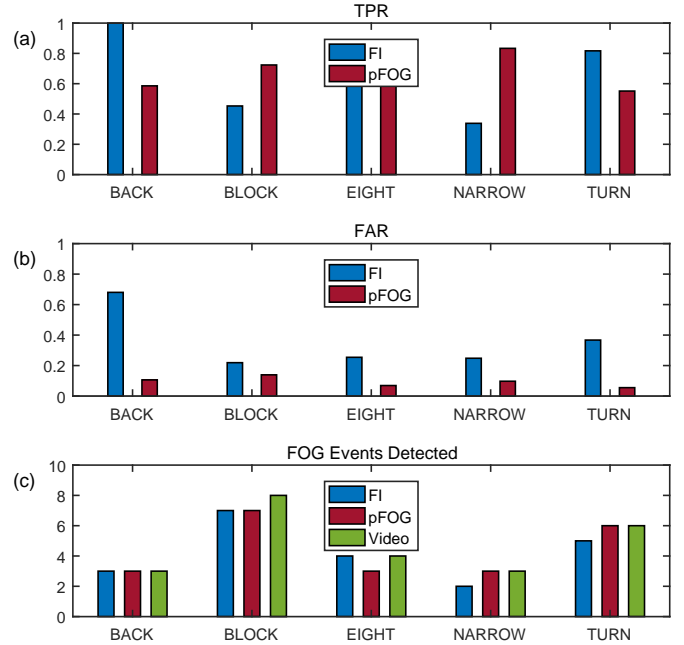


Fig. 11: Summary of TT027. (a) TPR, (b) FAR, and (c) FOG events detected.

The sum of the region identified as DL and MDL represents the FOG region detected in the video data.

For PID TT027, we choose the BLOCK task to obtain the FI-threshold and kernel parameter because the participant demonstrated the highest number of FOG events (equal to 8) in this task. We set the FI-threshold to 6.0 and the kernel parameter $\sigma_s = 0.29$ such that the number of FOG events detected is maximized. In Fig. 6-10, we plot the yaw angle of the motion of the left foot with an overlay of the DL, MDL, and FAL regions obtained using the video reference system. We notice that the FI-threshold obtained using the BLOCK task demonstrates high FAR in the remaining tasks. However, the proposed pFOG method demonstrates an improved accuracy with low FAR.

In Fig. 11, we summarize the results obtained for PID TT027. The FI-method detected 21/24 (or equivalently 87.5% accuracy) FOG events, whereas the pFOG method detected 22/24 (or equivalently 91.66% accuracy) FOG events. The average values of TPR for FI and pFOG method were 0.67

TABLE 1: Number of FOG events detected for different participants across the gait tasks.

PID	PARAMETER		BACK		BLOCK		EIGHT		NARROW		TURN		TOTAL	
	FI	pFOG	FI	pFOG	FI	pFOG	FI	pFOG	FI	pFOG	FI	pFOG	FI	pFOG
TT003	6.56	0.30	(0/0)	(0/0)	(0/1)	(0/1)	(0/0)	(0/0)	(0/0)	(0/0)	(0/0)	(0/0)	(0/1)	(0/1)
TT004	6.56	0.30	(0/2)	(1/2)	(0/6)	(4/6)	(0/0)	(0/0)	(0/0)	(0/0)	(0/0)	(0/0)	(0/8)	(5/8)
TT005	6.56	0.30	(0/1)	(1/1)	(0/0)	(0/0)	(0/0)	(0/0)	(0/1)	(1/1)	(0/0)	(0/0)	(0/2)	(2/2)
TT007	6.56	0.30	(8/8)	(4/8)	(0/0)	(0/0)	(0/1)	(1/1)	(1/1)	(0/1)	(0/0)	(0/0)	(9/10)	(5/10)
TT013	6.56	0.30	(0/0)	(0/0)	(1/3)	(2/3)	(0/0)	(0/0)	(1/2)	(0/2)	(0/0)	(0/0)	(2/5)	(2/5)
TT017	6.56	0.30	(0/0)	(0/0)	(1/1)	(0/1)	(0/0)	(0/0)	(0/0)	(0/0)	(0/0)	(0/0)	(1/1)	(0/1)
TT021	6.56	0.30	(1/1)	(1/1)	(1/3)	(3/3)	(0/2)	(1/2)	(0/0)	(0/0)	(0/1)	(1/1)	(2/7)	(6/7)
TT027	6.56	0.30	(3/3)	(3/3)	(5/8)	(7/8)	(4/4)	(3/4)	(2/3)	(3/3)	(5/6)	(6/6)	(19/24)	(22/24)
TOTAL	6.56 (avg)	0.30 (avg)	(12/15)	(10/15)	(8/22)	(16/22)	(4/7)	(5/7)	(4/7)	(4/7)	(5/7)	(7/7)	(33/58)	(42/58)

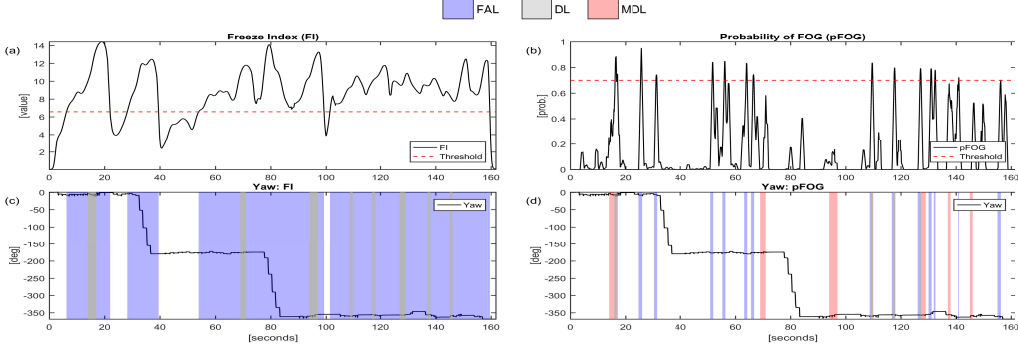


Fig. 12: PID TT007-BACK. (a) Freeze-Index plot with FI-threshold set to 6.56. (b) pFOG plot with $\sigma_s = 0.30$. (c) and (d) Yaw angle plot with an overlay of DL, MDL, and FAL. FOG region marked using the following video commentary: Festination backwards into freeze in the middle of first trial. Festination backwards into freeze at the end of the second trial. Six instances of festination backwards into freeze in the third trial.

and 0.65, respectively. However, our method demonstrates a lower average FAR of 0.09 when compared with the existing method which gives an average FAR of 0.35, indicating a four-fold reduction in the false alarm rate using the proposed method.

APPENDIX G EXPERIMENTAL EVALUATION: FIXED THRESHOLDS

In Table 1, we analyzed the accuracy of the existing and proposed method across different datasets for a fixed value of FI-threshold and σ_s . These fixed values are obtained by taking the average of the participant-specific FI-threshold and participant-specific kernel parameter in Table III of the original manuscript. In our analysis, we fix the FI-threshold to 6.56 and $\sigma_s = 0.30$. Overall, the pFOG method obtained an accuracy of 72.41%, i.e., 42/58 FOG events were detected using a fixed participant-specific kernel parameter (see Table 1). The FI method obtained an accuracy of 56.68%, i.e., 33/58 FOG events were detected using a fixed FI-threshold. In contrast, when the participant-specific parameters were manually adjusted, we obtained an accuracy of 70.68% and 81.03% for the FI method and pFOG method, respectively (see Table III of the original manuscript).

In Table 2, we report the performance of the FI method and proposed approach for a fixed value of the FI-threshold and participant-specific tunable parameter, respectively, across different types of freezing of gait. We notice that the proposed method performs better than the existing approach in detecting all types of freezing, except festination. However, for this particular type of freezing of gait, the false-alarm length

detected in the FI method is significantly higher than the proposed approach. In Fig. 12, we overlay the detection length (DL), missed detection length (MDL), and false alarm length (FAL) regions detected on the yaw angle plot obtained by the foot-mounted inertial navigation system for PID TT007-BACK trial (the only participant who demonstrated festinating gait). The definitions of DL, MDL, and FAL can be found in section VI-B of the main manuscript. We notice that the FI method detects large FAL (represented with blue background) for a fixed value of FI-threshold.

TABLE 2: Detection performance for different types of FOG events..

Event type (No. of events)	(not tuned) FI	(not tuned) pFOG
Turn Freeze (38)	47.36% (18)	76.31% (29)
Initiation/Gait Freeze (12)	58.33% (7)	75.00% (9)
Festination with Freeze (8)	100.00% (8)	50.00% (4)
Overall (58)	56.68% (33)	72.41% (42)